Research Square

Preprints are preliminary reports that have not undergone peer review.
They should not be considered conclusive, used to inform clinical practice,
or referenced by the media as validated information.

In-catalysts based on porous aromatic frameworks for the liquid-phase CO2 hydrogenation to methanol

Daria Makeeva

d-makeeva95@yandex.ru

Lomonosov Moscow State University

Alina Bikbaeva

Lomonosov Moscow State University

Anton Maximov

A.V. Topchiev Institute of Petrochemical Synthesis

Research Article

Keywords: hydrogenation, CO2, methanol, porous aromatic frameworks, indium nanoparticles

Posted Date: November 3rd, 2026

DOI: https://doi.org/10.21203/rs.3.rs-11317730/v1

License: This work is licensed under a Creative Commons Attribution 4.0 International License.
Read Full License

Additional Declarations: No competing interests reported.

In-catalysts based on porous aromatic frameworks for the liquid-phase CO_2 hydrogenation to methanol

Daria Makeeva[1,2,*], Alina Bikbaeva[1], Anton Maximov[1,2]

[1] Department of Petroleum Chemistry and Organic Catalysis, Faculty of Chemistry, Lomonosov Moscow State University, 1-3 Leninskiye Gory, Moscow 119991, Russia

[2] Topchiev Institute of Petrochemical Synthesis, RAS (TIPS RAS), Moscow 119991, Russia

*Corresponding author E-mail: d-makeeva95@yandex.ru

Postal address: Lomonosov Moscow State University, Faculty of Chemistry, Department of Petroleum Chemistry and Organic Catalysis, 1-3 Leninskiye Gory, Moscow, Russia, 119991

Daria Makeeva, ORCID: https://orcid.org/0000-0001-7750-7457
Alina Bikbaeva, ORCID: https://orcid.org/0009-0008-1493-0651
Anton Maximov, ORCID: https://orcid.org/0000-0001-9297-4950

Abstract

The catalytic hydrogenation of carbon dioxide into valuable petrochemical products and fuel components is a promising approach to its utilization. One of the most important products of this reaction is methanol, which is used both for the production of various chemicals and as an alternative fuel. Recently, In-based catalysts have emerged as promising systems for the hydrogenation of CO_2 to methanol. However, the challenge of tuning the morphology of the active phase particles and selecting suitable supports and media for efficient catalytic performance remains a key issue. Herein, In-catalysts based on the porous aromatic framework PAF-20 and its aminated analogue PAF-20-NH_2 were synthesized and tested in the liquid-phase hydrogenation of CO_2 to methanol for the first time. The structure of the materials and catalysts was established using low temperature N_2 adsorption, elemental analysis, FTIR spectroscopy, TEM and XPS. According to XPS data, a short reduction time facilitates the formation of oxygen vacancies in the structure of In-catalysts. The influence of reaction temperature, hydrogen pressure, indium content, and reaction media on the catalytic activity was systematically studied. In–PAF-20 demonstrated the highest methanol production rate of 435 mg_{MeOH} g_{In}^{-1} h^{-1} at 60 atm and 275°C, while in a subcritical ethanol In–PAF-20-NH_2 exhibited methanol production rate of 507 mg_{MeOH} g_{In}^{-1} h^{-1}. Both catalysts retained their activity over five reuse cycles.

Keywords: hydrogenation, CO_2, methanol, porous aromatic frameworks, indium nanoparticles

Abbreviations

PAFs	Porous aromatic frameworks
MTBE	Methyl tert-butyl ether
PPP	Pyridylphenylene polymer
DMF	Dimethylformamide
THF	Tetrahydrofuran
BET	Brunauer–Emmett–Teller
NLDFT	Non-local density functional theory
FTIR	Fourier transform infrared
TEM	Transmission electron microscopy
XRF	X-ray fluorescence
XPS	X-ray photoelectron spectroscopy
BE	Binding energy
RWGS	Reverse water-gas shift reaction

Declarations

Ethics and Consent to Participate Not applicable.

Consent for Publication Not applicable.

Conflict of Interest The authors declare that they have no known competing financial interests or personal relationships that could have appeared to influence the work reported in this paper.

Author Contributions Daria Makeeva: investigation, analysis, writing - original draft. Alina Bikbaeva: investigation, writing - original draft. Anton Maximov: formal analysis, writing - review and editing, supervision.

Funding This work was supported by the Russian Science Foundation [grant number 24-13-00242].

Data Availability No data was used for the research described in the article. The experimental data are provided in the main manuscript.

1 Introduction

High rates of consumption of fossil resources (oil, coal, and natural gas) result in significant emissions of carbon dioxide, the main greenhouse gas contributing to climate change [1]. Currently, the primary approaches to reduce CO_2 emissions are the optimization of industrial processes or its capture and subsequent disposal in underground storage facilities [2]. However,

the latter method is associated with high investment costs, the risk of leaks, and limitations in the choice of storage locations. Therefore, CO_2 capture and its subsequent processing into valuable chemicals and fuels appears particularly promising. One of the main methods of CO_2 conversion is its catalytic hydrogenation into methanol, formic acid, diethyl ether, etc. [3]

Among them, methanol is of particular interest because it is a basic feedstock for a wide range of commonly used chemical products: high-octane motor fuel components (such as MTBE), dimethyl ether, dimethyl carbonate, formaldehyde, olefins, and other compounds [4]. Moreover, methanol can be used as an alternative fuel and energy source, and plays a key role in the green hydrogen production chain, serving as a convenient and safe form of storage and transportation.

In industry, methanol is produced primarily from natural gas via the syngas production stage. Although the use of existing production capacities for direct CO_2 conversion seems rational, this process is significantly restricted thermodynamically [5]. Under standard conditions, the hydrogenation of CO_2 to methanol is characterized by a small positive standard Gibbs free energy (ΔG_{298K} = +3.5 kJ/mol), with equilibrium shifting toward methanol formation at lower temperatures and higher pressures. At the same time, acceptable process rates require increased temperatures.

Nowadays, pilot plants for CO_2 hydrogenation to methanol mostly operate on well-known Cu-ZnO-Al_2O_3 catalysts used to produce methanol from syngas [6]. Cu-based catalysts are known for their high activity; however, they are still characterized by limited methanol selectivity and stability. Recently, reducible oxide catalysts such as In_2O_3 and $ZnZrO_x$ emerged as alternative systems for CO_2 hydrogenation and gained significant attention due to their high selectivity and stability [7, 8]. Indium oxide is primarily used in its bulk form; however, its inherent H_2 activation ability and overall activity are rather low [9]. The ways to improve In_2O_3 catalytic performance include the use of promoters (Pd, Ni, Pt, etc.) for enhanced H_2 activation or supports for the active phase stabilization and the improvement of its dispersion [10].

To date, relatively few studies have been devoted to supported In-catalysts. The majority of them describe catalytic systems based on inorganic supports, such as SiO_2 [11], CeO_2 [12], and ZrO_2 [8, 13]. The latter has received particular attention, as it promotes dispersion of indium oxide, contributes to an increase in the concentration of oxygen vacancies at the In_2O_3–ZrO_2 interfaces, and to the adsorption and activation of CO_2. It should be noted that catalysts based on In_2O_3 nanoparticles supported on carbon materials have not been described in the literature yet. However, in a study [14] In-catalysts based on a hybrid support consisting of silicon oxide modified with hyperbranched pyridylphenylene polymer (PPP) were synthesized for the hydrogenation of CO_2 to methanol. It was shown that this modification of the support facilitated additional adsorption of

CO_2, promoted stabilization of reaction intermediates, and prevented reduction and aggregation of In_2O_3 nanoparticles.

Based on the above, the use of porous organic polymers, particularly porous aromatic frameworks (PAFs), as supports for In-nanoparticles appears novel and promising. PAFs are 3D-structures consisting of aromatic rings linked by covalent C-C bonds and characterized by high thermal stability, high specific surface area, and developed porosity. A wide range of well-known modification procedures is also available for PAFs, which is important, as it was shown before that functional groups contribute to the stabilization of transition metal nanoparticles and complexes within their structure [15–17]. Previously, PAFs-based catalysts have been studied in various processes including the hydrogenation of unsaturated compounds [18, 19], lignin-cellulose biomass components [20–22] and organic carbonates [23, 24], oxidation [25, 26], hydroformylation [27], etc.

It should also be noted that CO_2 hydrogenation is predominantly carried out in the gas phase [28]. Although the liquid-phase process has been less extensively studied, it is of significant interest because the use of a solvent facilitates efficient heat removal, shifts the reaction equilibrium toward methanol formation through the dissolution of methanol and water and therefore contributes to the alleviation of reaction conditions [29, 30]. Heterogeneous catalytic systems used in liquid-phase hydrogenation described in the literature can be categorized primarily into Cu- [31], Pd- [32], and Mo_2C-based [33] catalysts, whereas In-based catalysts remain virtually unstudied.

In this work, In-catalysts based on porous aromatic frameworks were obtained and investigated in the liquid-phase hydrogenation of CO_2 to methanol for the first time. The dependence of the active phase morphology on the support structure and the presence of amino groups was examined, as was the relationship between these parameters and catalytic activity.

2 Experimental section

2.1 Materials

The following reagents were used in this work: *tetrakis*(4-bromophenyl)methane (synthesized according to the method described in [34]), 1,4-phenylenediboric acid ($(HO)_2$B-Ph-B$(OH)_2$, ABCR, 96%), triphenylphosphine (PPh_3, Aldrich, ReagentPlus®, 99%), potassium carbonate (K_2CO_3, Reakhim, high-purity grade), palladium (II) acetate ($Pd(OAc)_2$, Aldrich, 99.9%), nitric acid (HNO_3, Component-Reaktiv LLC, reagent grade), trifluoroacetic acid (CF_3COOH, Aldrich, ReagentPlus®, 99%), tin (II) chloride dihydrate ($SnCl_2$ x $2H_2O$, Aldrich,

98%), hydrogen peroxide (H_2O_2, Prime Chemicals Group, 50 wt% aqueous solution), hydrochloric acid (HCl, Sigma-tech, high-purity grade), indium (III) nitrate 4.5-aqueous ($In(NO_3)_3$ x $4.5H_2O$, Khimkraft, 99%), hydrogen (H_2, PGS LLC, 99.99%), carbon dioxide (CO_2, PGS LLC, 99.99%).

The following solvents were used: dimethylformamide (DMF) ($HC(O)NMe_2$, Ruskhim, high-purity grade), ethanol (C_2H_5OH, IREA 2000, purum p.a.), tetrahydrofuran (THF) (C_4H_8O, Khimmed, high-purity grade), 1,4-dioxane ($C_4H_8O_2$, Ruskhim, high-purity grade), dichloromethane (CH_2Cl_2, Component-Reaktiv LLC, high-purity grade).

2.2 Characterizations

IR spectra were recorded in the 4000–500 cm^{-1} range on a Nicolet IR-200 instrument (Thermo Scientific) using the multiple attenuation total reflection method with a Multi-Reflection HATR accessory containing a 45° ZnSe crystal for various wavelength ranges with a resolution of 4 nm.

Nitrogen adsorption-desorption isotherms were recorded at 77 K on a Gemini VII 2390 (V1.02t) instrument (Micromeritics). Before measurements, the samples were degassed at 120°C for 8 h. Surface area was calculated using the Brunauer–Emmett–Teller (BET) model based on adsorption data in the relative pressure range $p/p_0 = 0.05–0.2$. Total pore volume was determined based on the amount of nitrogen adsorbed at a relative pressure of $p/p_0 = 0.96$. Pore size distribution for all obtained samples was calculated with SAIEUS software using a 2D-NLDFT model for N_2 adsorption on carbon materials with standard slit pores.

Transmission electron microscopy (TEM) analysis of the catalysts was performed on a JEOL JEM-2100 instrument with a magnification of 50 to 1500000 and an image resolution of 0.19 nm. The electron beam potential was 200 kV. Micrographs were processed using ImageJ software.

The metal content of the catalysts was determined by X-ray fluorescence (XRF) analysis on a Spektroskan MAX-GVM spectrometer (NPO Spektron) at the Laboratory for Microanalysis of INEOS RAS.

X-ray photoelectron spectroscopy (XPS) studies of the catalysts were performed on a VersaProbe II PHI 5000 instrument. Monochromatic Al Kα radiation (hν = 1486.6 eV) with a power of 50 W was used to excite photoemission. The instrument's binding energy scale was calibrated using the Au 4f (84.0 eV) and Cu 2p3/2 (932.6 eV) lines. The energy analyzer's pass energy for individual lines was 23.5 eV. Photoelectron peaks were calibrated using the carbon C 1s line with a binding energy of 284.5 eV.

Gaseous product analysis was performed by gas chromatography on a Crystallux-4000 M instrument (NPF Meta-Khrom LLC) equipped with a Carboxen-1000 packed column (5 m, 60/80

mesh) and a thermal conductivity detector. Argon was used as the carrier gas. Chromatograms were recorded and analysed using specialized software.

The reaction products were analyzed by gas-liquid chromatography on a Hewlett-Packard chromatograph equipped with a flame ionization detector and a 30 m × 0.32 mm × 0.5 μm column (DB-WAX bonded phase). Hydrogen was used as a carrier gas. Chromatograms were recorded and analyzed on a computer using HP ChemStation Rev. A. 06. 01 (403) software. The methanol yield was determined using 1,4-dioxane as an external standard.

2.3 Material and catalyst synthesis

2.3.1 Synthesis of PAF-20 (adapted from [35])

Tetrakis(4-bromophenyl)methane (2 g, 3.14 mmol) and 1,4-phenylenediboric acid (1.04 g, 6.27 mmol) were dissolved in 100 mL of DMF in a 250 mL single-neck flask equipped with a magnetic stirrer bar, then 2M K_2CO_3 solution (13 mL, 26 mmol), palladium (II) acetate (70.6 mg, 0.314 mmol) and triphenylphosphine (452 mg, 1.726 mmol) were added to the mixture while stirring. The solution was degassed using the freeze-pump-thaw method, after which the flask was equipped with a reflux condenser, and the reaction was carried out with vigorous stirring for 24 hours at 140°C. The resulting precipitate was filtered, washed with water (2 x 50 ml), and transferred to a 100 ml beaker, where it was treated for 40 minutes with a solution of concentrated HCl (40 ml) in water (40 ml) with the addition of 300 μl of H_2O_2 to remove residual Pd. The precipitate was then filtered again and washed with water (2 x 50 ml), ethanol (50 ml), dichloromethane (50 ml), and ethanol once more (50 ml). After drying under vacuum for 6 hours, a white powder of the porous aromatic framework PAF-20 (1.62 g) was obtained.

2.3.2 Synthesis of PAF-20-NO_2 (adapted from [36])

Trifluoroacetic acid (50 mL) was placed in a 100 mL three-neck flask installed in an ice bath and equipped with a magnetic stirrer bar, reflux condenser, and dropping funnel. The flask was cooled to 0°C. PAF-20 (1 g) was added afterwards and stirred for 10 minutes, then 350 μL of nitric acid was added dropwise. The reaction mixture was stirred at room temperature for 8 hours. The resulting suspension was poured into ice, washed with water (2 x 50 ml), ethanol (2 x 50 ml), and THF (50 ml), and then dried under vacuum for 6 hours. The resulting product was a yellow powder (915 mg).

2.3.3 Synthesis of PAF-20-NH_2 (adapted from [36])

In a 250 mL round-bottomed flask equipped with a magnetic stirrer bar and reflux condenser, 0.7 g of PAF-20-NO_2 was dispersed in 150 mL of THF. Tin (II) chloride (11 g, 48.7 mmol) was then added. The reaction mixture was stirred at reflux for 8 hours, afterwards the mixture was cooled and filtered. To remove the tin residue the resulting precipitate was placed in a 50 mL of 10% NaOH solution and stirred for 30 min. Then it was filtered again, washed with water (2 x 50 ml), and treated for 40 minutes with a solution of concentrated HCl in water (40/40 ml) with the addition of 300 µl of H_2O_2. The precipitate was then washed with water (2 x 50 ml) and ethanol (2 x 50 ml) and dried under vacuum for 8 hours. The resulting product was an orange powder (638 mg).

2.3.4 Synthesis of In-PAF catalysts

In a 50 ml single-neck flask equipped with a magnetic stirrer bar, 10.3 mg of indium(III) nitrate was dissolved in 50 ml of ethanol. Then, 100 mg of PAF was added and the mixture was stirred for 24 hours at room temperature. The resulting suspension was dried under vacuum for 6 hours. To reduce the resulting powder with hydrogen, the entire catalyst mass was loaded into a 2 cm diameter, 33 cm long quartz reactor and reduced at atmospheric pressure under a hydrogen flow of 1.5 L/h for 0.5 hours at 300°C, heating at 3°C/min.

2.4 Catalytic tests

The hydrogenation reactions were carried out in a steel autoclave equipped with a magnetic stirrer bar. 15 mg of catalyst and 4.5 ml of solvent were added to the autoclave, which was then sealed, filled with CO_2 and H_2 in a 1:3 ratio, respectively, and placed in an oven preheated to the required temperature. Upon completion of the reaction, the autoclave was cooled below room temperature and then depressurized. The reaction products were analyzed by gas and gas-liquid chromatography. The methanol production rate was calculated based on the following equation:

$$W = \frac{m_{(CH_3OH)}}{m_{(Me)} \times t},$$

where $m(CH_3OH)$ is the amount of obtained methanol in mg, $m(Me)$ is the amount of catalytically active metal loaded into the catalytic reaction in g, and t is the reaction time in h.

In the recycling experiments, reaction was finished after the first run, the used catalyst was recovered by centrifugation and washed with ethanol, followed by centrifugation. The process was repeated twice, and the resultant solid was used directly in the next run with the same amount of fresh solvent.

3 Results and Discussion

3.1 Synthesis and characterization of PAFs

Porous aromatic frameworks PAF-20 (also known as PPAF-1 [36]) and its amino-modified derivative PAF-20-NH_2 (also known as PPAF-NH_2 [36]) were synthesized using the techniques described before in [15, 35, 36]. PAF-20 was prepared via Suzuki-Miyaura cross-coupling between 1,4-phenylenediboronic acid and *tetrakis*(4-bromophenyl)methane with $Pd(PPh_3)_4$ as the catalyst formed *in situ* from $Pd(OAc)_2$ and PPh_3 (Fig. 1). PAF-20 was further treated with the mixture of nitric and trifluoroacetic acids followed by the reduction with tin (II) chloride to obtain PAF-20-NH_2 (Fig. 1). It was shown previously, that the number of benzene rings between the carbon nodes in the PAFs structure defines the textural characteristics of materials, thus, the use of shorter linkers results in the higher surface areas [18]. This may play an important role in the case of hydrogenation of small gas molecules, since a more developed surface may improve catalytic efficiency.

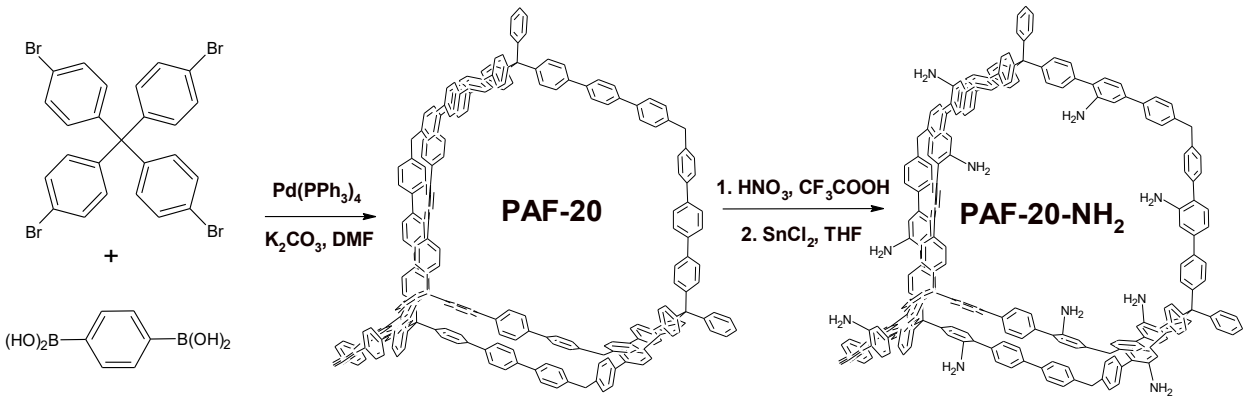


Fig.1 Schematic synthesis of PAFs obtained in current work

The structural properties of the obtained materials were studied using IR spectroscopy and low-temperature nitrogen adsorption-desorption.

IR spectroscopy was used to monitor the extent of the framework functionalization (Fig. 2). The IR spectra of the initial PAF-20 demonstrate the absence of signals in the regions of 3300–

3400 cm^{-1} and 1076 cm^{-1}, characteristic of B–OH and C–Br bond vibrations, respectively, indicating complete cross-coupling between the starting monomers. The appearance of absorption bands at 1527 and 1344 cm^{-1} in the IR spectrum of the PAF-20-NO_2, attributed to asymmetrical and symmetrical N–O stretches of nitro groups [37], confirms the successful functionalization of the framework. These bands disappear in the IR spectrum of PAF-20-NH_2, while a new absorption band with a maximum at 1616 cm^{-1} appears, corresponding to the N–H bond deformation vibrations of amino groups [38] and indicating complete reduction of nitro groups.

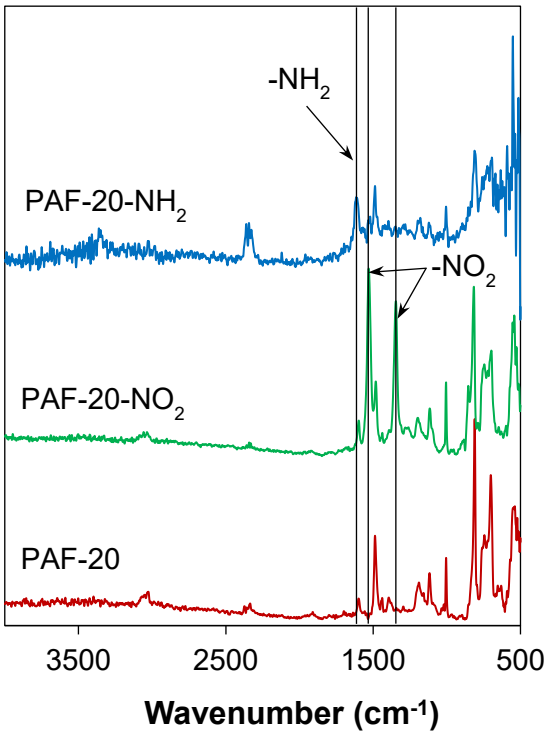


Fig.2 IR-spectra of PAFs obtained in this work

The textural characteristics of synthesized supports were studied using low-temperature nitrogen adsorption-desorption (Table 1). For PAF-20-NH_2 a decrease in specific surface area was observed compared to the initial PAF-20 due to the introduction of functional groups into their structure.

Table 1 Textural properties and elemental composition of PAFs synthesized in this work

№	Material	S_{BET}, m^2/g	$V_{tot.}$, cc/g	ω(N), wt.%
1	PAF-20	520	0.34	-
2	PAF-20-NH_2	388	0.22	5.8

The nitrogen adsorption isotherms of the obtained materials are characterized by intense adsorption in the region of low relative pressures (p/p_0 = 0–0.05) indicating the presence of a microporous structure (Fig. 3). Both a gradual rise in the adsorption isotherm in the range of relative pressures p/p_0 = 0.2–0.9 and a hysteresis loop between the adsorption and desorption curves demonstrate the presence of mesopores in the structure of the obtained polymers. The isotherm shape is mostly preserved for PAF-20-NH_2 compared to the initial PAF-20. The main differences include reduced adsorption and a narrowing of the hysteresis loop resulting from the partial filling of pores with amino groups and their consequent narrowing.

An open hysteresis loop should also be noted for both frameworks, which may be associated with the formation of ultramicropores, due to interpenetration of the framework domains [39]. This phenomenon is characteristic of certain heterogeneous porous supports, such as metal-organic and covalent organic frameworks [40, 41].

The pore size distribution (Fig. 3) was calculated using the NLDFT method based on the adsorption branch of the nitrogen isotherms. The resulting pore size distributions indicate a predominantly microporous structure with maxima at 1.0 nm and 0.9 nm for PAF-20 and PAF-20-NH_2, respectively. Moreover, a small amount of mesopores is also observed in the range of 2–4 nm for both materials.

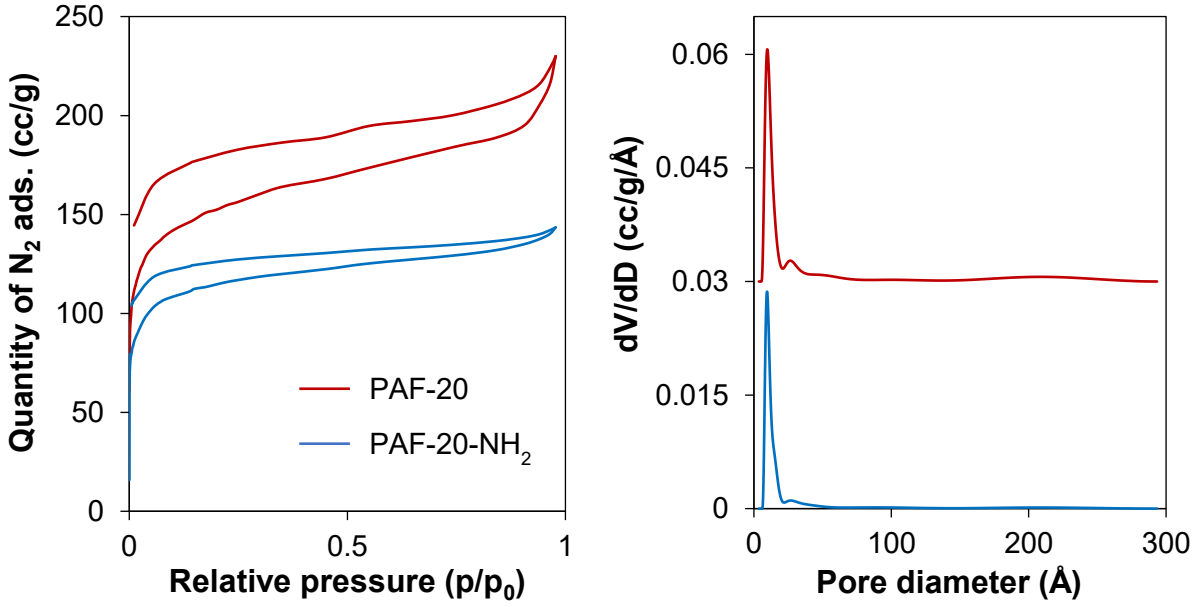


Fig.3 Nitrogen adsorption-desorption isotherms and pore size distribution graphs for PAF-20 and PAF-20-NH_2 materials

3.2 Synthesis and characterization of the catalysts

Monometallic In-containing catalysts In–PAF-20 and In–PAF-20-NH_2 were synthesized by impregnating the support with an $In(NO_3)_3$ solution in ethanol, followed by solvent evaporation and subsequent reduction in a hydrogen stream. The obtained catalysts were characterized by TEM, XRF, low-temperature nitrogen adsorption-desorption, and XPS.

According to TEM data, In–PAF-20 and In–PAF-20-NH_2 catalysts are characterized by a uniform distribution of active phase nanoparticles within the aromatic framework structure (Fig. 4). Both samples exhibit a particle size distribution close to normal with maxima of 3.6 ± 0.9 nm and 4.4 ± 0.9 nm for In–PAF-20 and In–PAF-20-NH_2, respectively. These results indicate effective particle stabilization within the porous structure of the support. The increase in the average particle size in the case of the In–PAF-20-NH_2 catalyst may be associated not only with the influence of functional groups, but also with a higher metal content (Table 2).

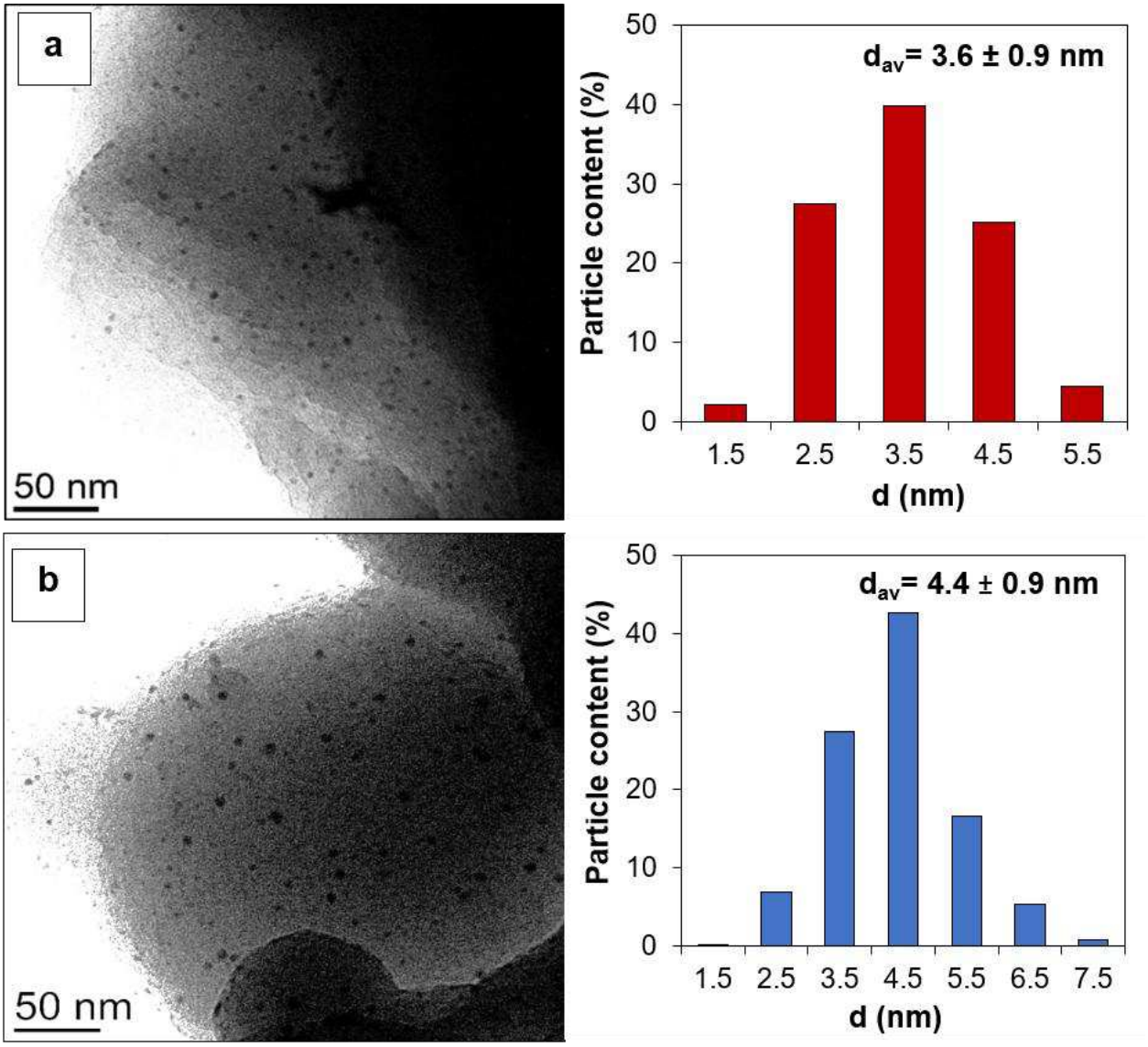


Fig.4 TEM microphotographs and particle size distribution graphs for **a** In–PAF-20, **b** In–PAF-20-NH_2

XRF data confirms that the metal content for both catalysts is close to the theoretical value of 3 wt.% (Table 2). In the case of In-PAF-20-NH_2 catalyst, the indium content was slightly higher, which may be attributed to the enhanced impregnation efficiency due to the formation of In(III) complexes with amino groups in the support structure [42, 43].

Table 2 Textural properties and elemental composition of catalysts synthesized in this work

№	Material	S_{BET}, m^2/g	$V_{tot.}$, cc/g	ω(In), wt.%
1	In-PAF-20	51	0.07	2.6
2	In-PAF-20-NH_2	333	0.21	3.0

The low-temperature nitrogen adsorption-desorption isotherms for the catalysts (Fig. 5) generally replicate the shape of the corresponding supports, indicating preservation of the porous structure after indium deposition. However, much lower nitrogen adsorption values were observed for the In–PAF-20 sample compared to In–PAF-20-NH_2 (Table 2). This is likely due to a partial blockage of the micropores and small mesopores by In-nanoparticles with the average diameters below 3 nm whose presence was confirmed by TEM data (Fig. 4a). For In–PAF-20-NH_2 the content of particles with such sizes is much smaller (Fig. 4b), therefore the micro-mesoporous system mostly remains unaltered. Meanwhile, a hysteresis loop between the adsorption and desorption curves became wider, indicating restricted nitrogen diffusion, which may also be related to partial pore blocking by active phase nanoparticles [44].

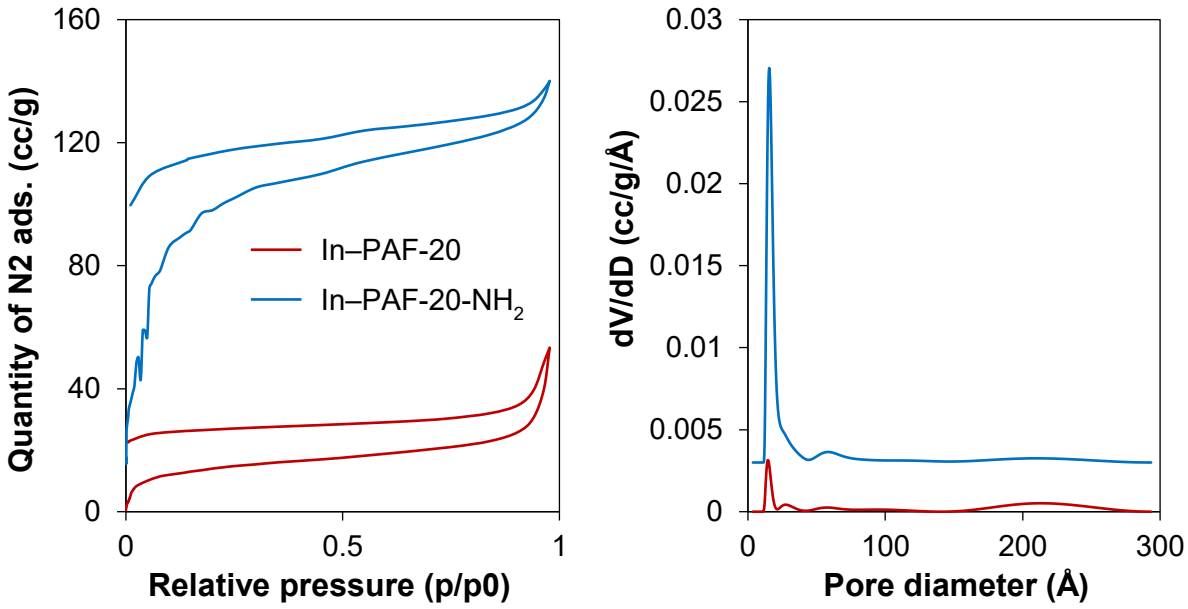


Fig.5 Nitrogen adsorption-desorption isotherms and pore size distribution graphs for In-PAF-20 and In-PAF-20-NH_2 catalysts

According to the XPS data for In–PAF-20 (Table 3, Fig. 6), the C 1s spectrum demonstrates one main signal at 284.5 eV, corresponding to the Csp^2–Csp^2 bond, as well as an accompanying π-π* satellite at 291.3 eV (Fig. 6a).

The O 1s high-resolution XPS spectrum was deconvoluted into three peaks at 530.4 eV, 532.2 eV, and 533.6 eV, corresponding to lattice oxygen, oxygen vacancies, and –OH groups, respectively (Fig. 6b) [45]. The peak at 532.2 eV, resulting from the In bonding with less than six O atoms (due to the formation of oxygen vacancies), is dominant in the spectrum (Table 3), indicating an extremely defective structure of the active phase closer in composition to hydroxylated indium oxide nanoparticles $In_2O_{3-x}(OH)_y$ [46]. A high content of defects may be associated with a small particle size (< 5 nm), short low-temperature reduction (heating at 3°C/min to 300°C, holding for 0.5 h), and partial hydration of the sample under the influence of moisture contained in the atmosphere [47]. It should be noted that oxygen vacancies in the structure of In-based catalysts play a key role, as they facilitate the effective adsorption of CO_2 via an oxygen atom, leading to the stabilization of the formate intermediate (HCOO*) and thereby directing the hydrogenation reaction along the formate pathway [9].

Analysis of the In 3d (Fig. 6c) spectrum indicates the presence of indium exclusively in the In^{3+} state. The two peaks at 445.4 and 445.9 eV can be assigned to In_2O_3 and $In(OH)_3$, respectively [48]. The content of hydroxide species in the In 3d spectrum (34%) correlates with the content of hydroxyl groups according to the O 1s spectrum (31%) (Table 3).

Table 3 Peak parameters for XPS spectra of obtained In-catalysts

Catalyst		**In–PAF-20**		**In–PAF-20-NH₂**	
Line	*State*	BE, eV	Content, %	BE, eV	Content, %
In 3d	In_2O_3	$3d_{5/2}$, 445.4 $3d_{3/2}$, 453.0	66	$3d_{5/2}$, 445.3 $3d_{3/2}$, 452.9	71
	$In(OH)_3$	$3d_{5/2}$, 445.9 $3d_{3/2}$, 453.5	34	$3d_{5/2}$, 446.0 $3d_{3/2}$, 453.7	29
O 1s	O_L	530.4	9	530.2	10
	O_V	532.2	60	532.0	62
	-OH	533.6	31	533.4	28
N 1s	C_{Ar}-NH_2	-	-	399.4	61
	C_{Ar}-$NH_2^{\delta+}$-In			400.4	39

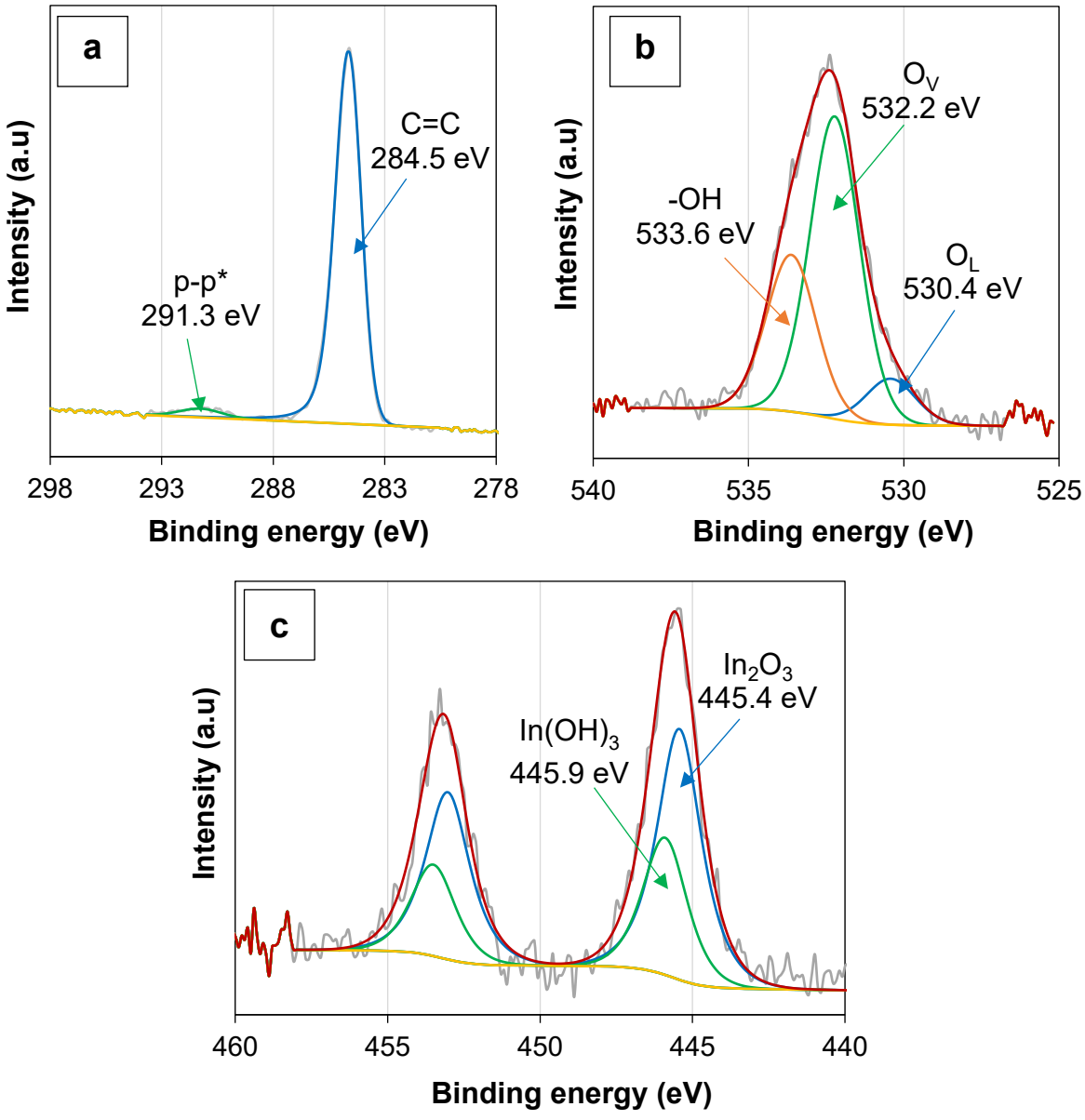


Fig.6 High resolution XPS spectra of **a** C 1s, **b** O 1s, and **c** In 3d for In-PAF-20

The C 1s spectrum for In–PAF-20-NH_2 (Fig. 7a) in addition to the signal at 284.5 eV corresponding to the Csp^2–Csp^2 bond and the characteristic π-π* satellite band at 291.3 eV exhibits a peak at 285.3 eV related to C–N bond. The N 1s spectrum contains two signals with maxima at 399.4 eV and 400.2 eV, corresponding to neutral amino groups and metal coordinated amino groups (Fig. 7b), which indicates the participation of functional groups in the stabilization of the active phase [49].

The O 1s (Fig. 7c) and In 3d (Fig. 7d) spectra are generally similar to those of In–PAF-20 catalyst. However, both O 1s and In 3d spectra components for In–PAF-20-NH_2 are shifted toward lower BE values relative to the BE values of the unmodified In–PAF-20 catalyst by 0.2 and 0.1 eV, respectively. The decrease in BE values for In–PAF-20-NH_2 catalyst may be attributed to both the electron-donating effect of amino groups in the support structure and the increase in particle size compared to the unmodified catalyst. Similar trends—albeit more pronounced—have previously been reported for Pd catalysts [18].

The hydroxyl component contents derived from the O 1s and In 3d XPS spectra for In–PAF-20-NH_2 catalyst coincided at ~29%, a value slightly lower than that observed for In–PAF-20 catalyst (Table 3). The In–PAF-20 catalyst particles are smaller (Fig. 4a), which may account for their more rapid hydroxylation during storage in air.

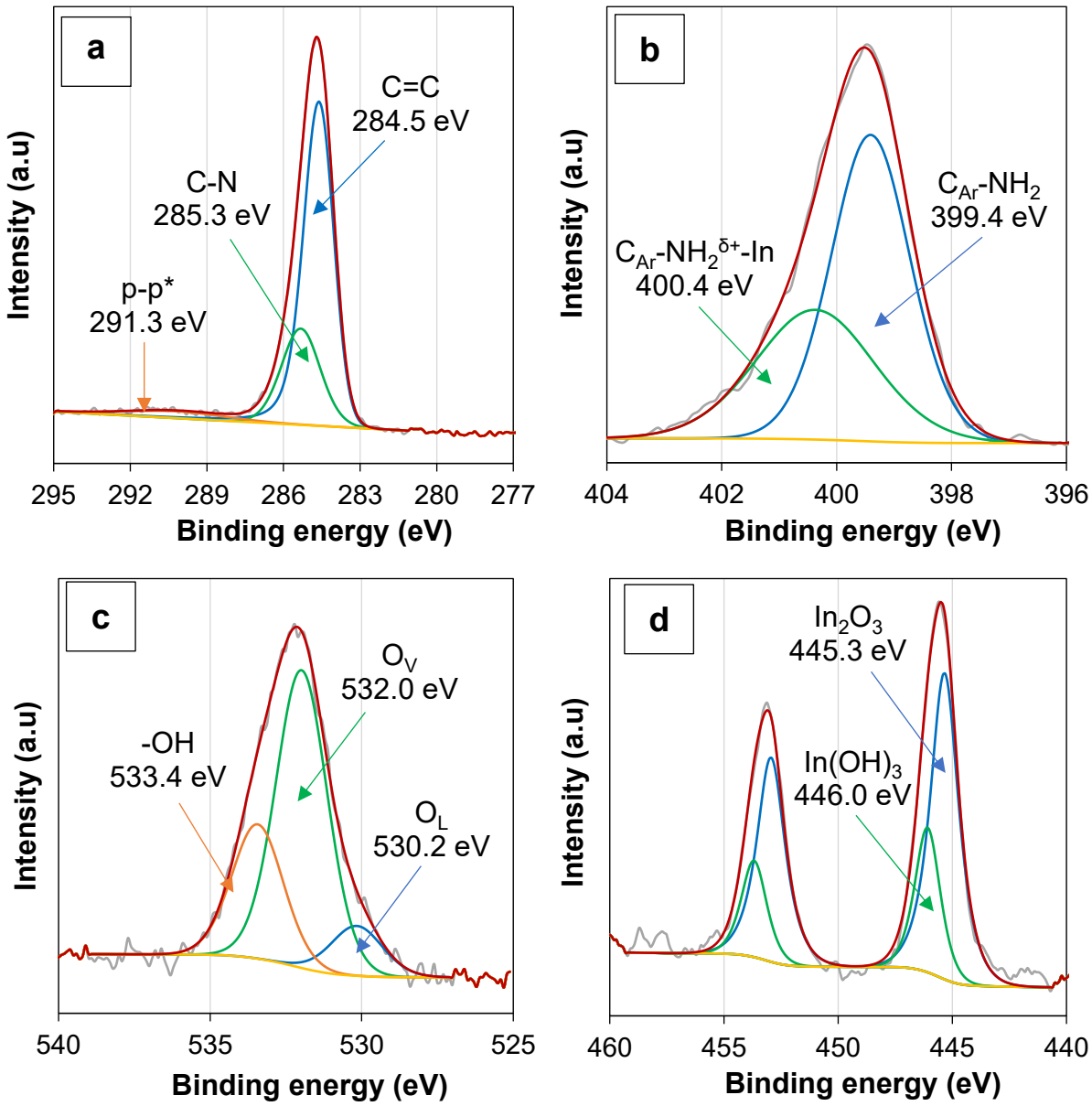


Fig.7 High resolution XPS spectra of **a** C 1s, **b** N 1s, **c** O 1s, and **d** In 3d for In-PAF-20-NH_2

3.3 Catalytic tests

First of all, the conditions for the CO_2 hydrogenation reaction were varied using the In-PAF-20 catalyst, taking into account stoichiometric considerations and general understanding of the thermodynamics and kinetics of the process. The CO_2/H_2 ratio was maintained at 3:1, which corresponds to the stoichiometry of methanol formation. While literature data primarily assesses the thermodynamic parameters of gas-phase reactions [7], this study focuses on the liquid-phase process, which can affect the equilibrium and kinetic parameters of the system. Therefore, the optimal reaction conditions were selected by experimentally varying key parameters: temperature, pressure, and In content. Ethanol was selected as the primary solvent for this study, because it had

previously been tested as a reaction medium for CO_2 hydrogenation [28]. According to the literature data, the introduction of alcohol solvents can enhance the reaction efficiency, primarily through the indirect conversion of CO_2 to methanol via formate intermediates [50]. Furthermore, the use of polar solvents facilitates the effective dispersion of PAFs. For all reactions described below, the gas phase composition was analyzed by gas chromatography. It should be noted that only H_2, CO_2, and air were detected in the gas phase; CH_4 and CO were not detected in the mixture, therefore the methanol selectivity was considered 100% in all cases.

The reaction temperature was varied between 225 and 300°C (Fig. 8a). With increasing temperature, a gradual increase in the methanol production rate from 331 to 404 $mg_{MeOH}\ g_{In}^{-1}\ h^{-1}$ was observed, which is consistent with the literature [12]. The reaction pressure was varied between 40 and 60 atm (Fig. 8b). The methanol production rate rose significantly from 363 to 455 $mg_{MeOH}\ g_{In}^{-1}\ h^{-1}$ upon increasing the pressure from 40 to 50 atm, respectively, after which the rise became less pronounced. This, on the one hand, is consistent with the thermodynamic data, and on the other, may also be due to increased CO_2 and H_2 solubility in the reaction medium and, consequently, an increase in the concentration of reactants at the active sites [7].

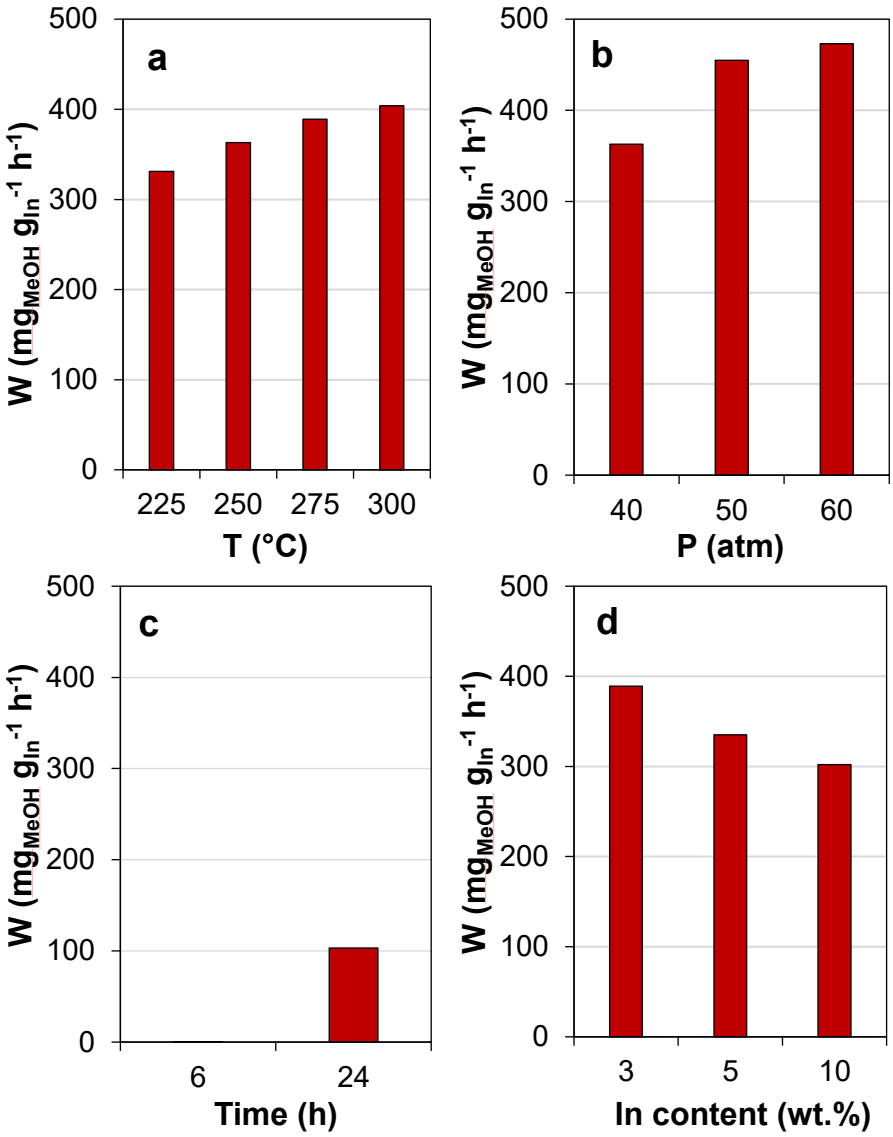


Fig.8 Dependence of the methanol production rate of the In-PAF-20 catalyst in the CO_2 hydrogenation to methanol on **a** temperature at 40 atm, **b** pressure at 250°C, **c** water medium at 250°C, 40 atm; and **d** In content at 275°C, 40 atm. *Reaction conditions*: In–PAF-20 – 15 mg, solvent – 4.5 mL, CO_2/H_2 = 1:3, 6 h

Additionally, the catalytic properties of In-PAF-20 were investigated in an aqueous medium (Fig. 8c). Under 250°C and 40 atm, the catalyst exhibited no activity at all after 6 h, and after the 24 hours the methanol production rate amounted to 103 mg_{MeOH} g_{In}^{-1} h^{-1}. A sharp decrease in activity in water compared to ethanol may be attributed to the hydrophobic nature of the support, which leads to limited catalyst dispersion and, consequently, restricts the accessibility of active sites. Furthermore, the reduced activity of the monometallic catalysts may stem from the aggregation of indium nanoparticles in water and excessive hydroxylation [12]. On the other hand, it has previously been demonstrated that the presence of co-adsorbed water during the process

helps to lower the energy barrier of the rate-limiting step of the formate mechanism [51], while water-ethanol mixtures can modulate reaction selectivity by suppressing the reverse water-gas shift (RWGS) reaction, thereby increasing the methanol yield [28].

The effect of metal content on the catalytic properties of the system was studied in the range of 3–10 wt.% (Fig. 8d). To ensure fair comparison, the mass of the active component was kept constant throughout the reactions, while the total mass of the catalyst was varied. The data obtained showed that the highest methanol production rate was achieved at a metal content of 3 wt.%, while a decrease in activity was observed with further increase in metal content.

Transmission electron microscopy was used to determine changes in the structure of the active phase (Fig. 9). According to the obtained data, the particle size distribution for the In-PAF-20 catalyst with a metal content of 5 wt.% was close to normal, with a maximum of 4.5 ± 0.9 nm. The formation of agglomerates with sizes of approximately 6.0-7.0 nm was also observed. Therefore, an increase in the In content led to a decrease in the dispersion of the active phase and its agglomeration, which contributed to a decrease in the methanol production rate, due to a decrease in the number of accessible active sites.

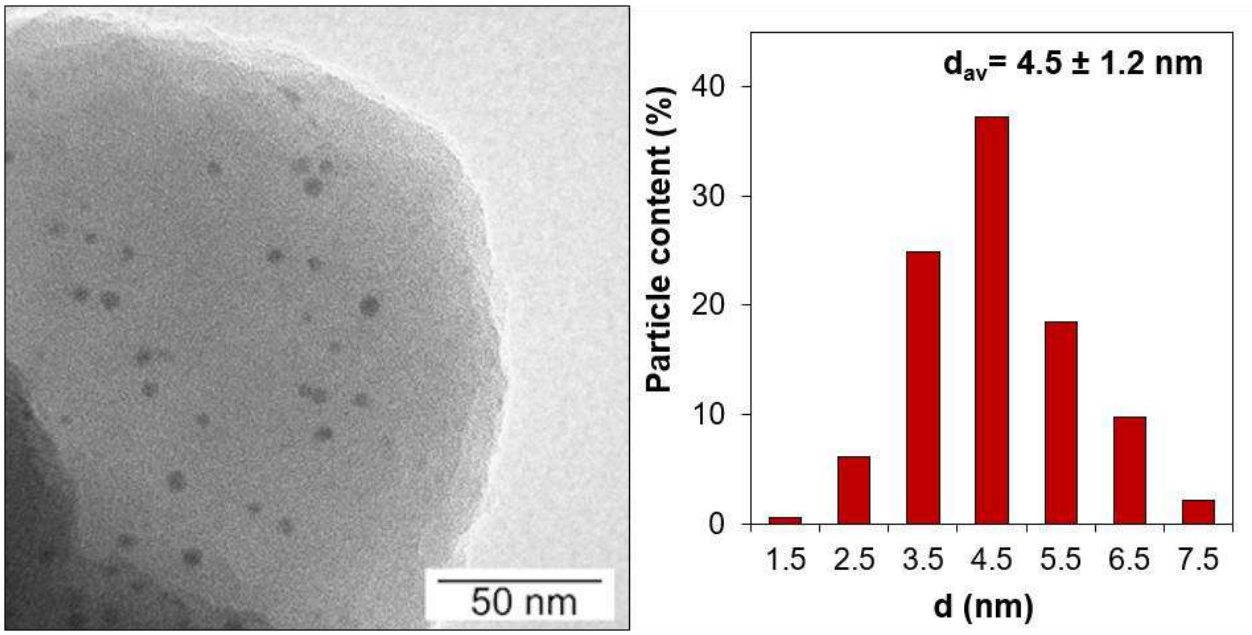


Fig.9 TEM microphotographs and particle size distribution for In–PAF-20 (5 wt.% In)

To compare the catalytic activity of the synthesized catalysts In–PAF-20 and In–PAF-20-NH_2, liquid-phase CO_2 hydrogenation reactions were conducted under several sets of conditions determined during preliminary studies. The catalysts were tested in order of intensifying reaction conditions: at first, at 40 atm and 250°C, then at 60 atm and 275°C and in the end, under conditions

of subcritical ethanol (Fig. 10). The data obtained allow us to evaluate the influence of support functionalization with amino groups and active phase morphology on the catalyst activity in CO_2 hydrogenation.

Analysis of the obtained data demonstrate that the rise in the methanol production rate of In–PAF-20-NH_2 upon transitioning from mild (40 atm, 250°C) to more elevated (60 atm, 275°C) conditions was relatively small – from 312 to 329 $mg_{MeOH}\ g_{In}^{-1}\ h^{-1}$, respectively. For In–PAF-20 the methanol production rate was higher in both cases – 363 and 435 $mg_{MeOH}\ g_{In}^{-1}\ h^{-1}$, respectively, and the increase was much more tangible.

According to XPS, the content of oxygen vacancies (Fig 6b, 7c) and In_2O_3 (Fig 6c, 7d) is quite similar for both catalysts, therefore observed phenomena is most likely related to the dispersion of the active phase. It is higher in the case of In–PAF-20 (Fig. 4a), which explains not only higher methanol production rates in case of both sets of conditions, but also their more pronounced increase. The lower activity of In–PAF-20-NH_2 may be related not only to its lower dispersion, but also to the partial blocking of active sites on the catalyst surface with amino groups. It is also known that CO_2 can react with amines to form carbamates and amides, which hinders its further conversion into methanol, since the hydrogenation of the intermediate products is not only the rate-limiting step but can also lead to the formation of N-methylation products rather than methanol [31, 52].

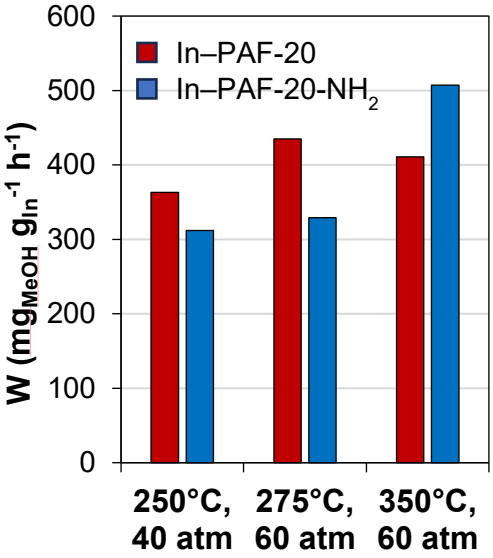


Fig.10 Comparison of the methanol production rates of catalysts obtained in this work in the hydrogenation of CO_2 to methanol. *Reaction conditions*: catalyst – 15 mg, ethanol – 4.5 mL, CO_2/H_2 = 1:3, 6 h

Furthermore, the activity of the obtained catalysts was studied in subcritical ethanol (Fig. 10). It should be noted that the hydrogenation of CO_2 to methanol using In-based catalysts under such conditions has not been previously described. Under these conditions, a change in the catalytic properties of the studied systems was observed. In particular, In–PAF-20-NH_2 demonstrated a higher methanol production rate of 507 mg_{MeOH} g_{In}^{-1} h^{-1} versus 411 mg_{MeOH} g_{In}^{-1} h^{-1} for In–PAF-20. It is known that under these conditions, the solvency of ethanol increases sharply, which ensures better diffusion of the reactants and promotes increased accessibility of the active sites of the catalyst [53]. Such conditions may also promote decomposition of intermediate carbamates and amides, therefore the contribution of CO_2 adsorption on amino groups becomes less significant, and although functional groups still contribute to the local concentration of CO_2 near the active phase, its further conversion to methanol at the active sites of the catalysts becomes preferential.

The reuse possibility was investigated over five consecutive cycles of CO_2 hydrogenation to methanol for both obtained catalysts (Fig. 11). In both cases the increase in the methanol production rate was observed after the 2nd cycle, which is more pronounced for In–PAF-20 and is most likely the result of the $In(OH)_3$ reduction to In_2O_3. However, for In–PAF-20 a significant decrease in the methanol production rate down to 392 mg_{MeOH} g_{In}^{-1} h^{-1} was observed after the fifth cycle. In–PAF-20-NH_2 demonstrated similar trend, however, the drop in its methanol production rate was less abrupt.

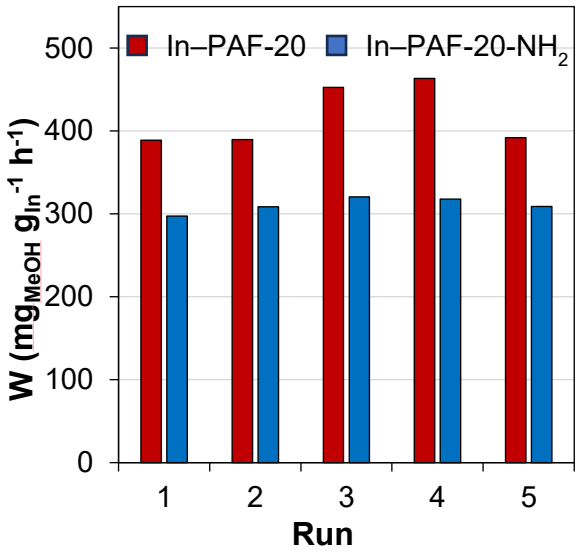


Fig.11 The methanol production rates of obtained catalysts upon reuse. *Reaction conditions*: catalyst – 15 mg, ethanol – 4.5 mL, 275°C, 60 atm, CO_2/H_2 = 1:3, 6 h

According to TEM data, the average particle size of the active phase for PAF-20 decreased slightly from 3.6 to 3.4 nm and the distribution was still close to normal after the fifth reaction run

(Fig. 12a). In contrast, the average particle size for In–PAF-20-NH_2 increased from 4.4 to 4.8 nm (Fig. 12b), and the content of particles larger than 7 nm also rose significantly. It was demonstrated in our previous works that the incorporation of amino groups in the structure of PAF promotes higher dispersion and additional stabilization of the active phase for other transition metals, such as Pd [15], Ru [20], Cu [23], however, the opposite trend was observed for In-based catalysts in this study.

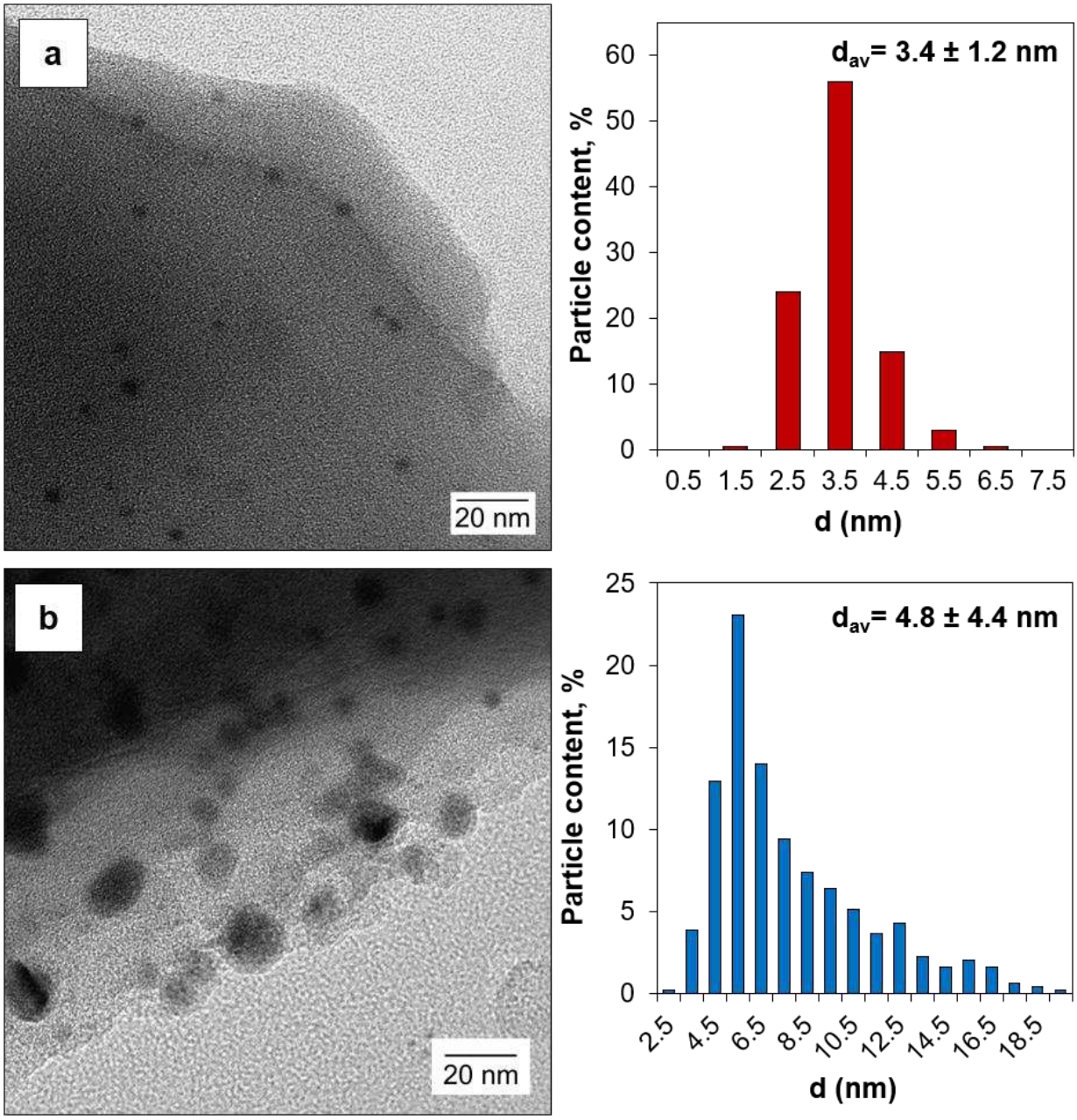


Fig.12 TEM microphotographs and particle size distributions for **a** In–PAF-20, **b** In–PAF-20-NH_2 after the 5th reuse cycle

4 Conclusions

Thus, this study reports the first synthesis of In-based catalysts supported on porous aromatic frameworks, both unmodified (PAF-20) and amino-functionalized (PAF-20-NH_2). It was found that using PAFs as supports enables the preparation of highly dispersed catalysts with average particle sizes of 3.6 and 4.4 nm for In–PAF-20 and In–PAF-20-NH_2, respectively. According to XPS data, both catalysts were characterized by a high content of oxygen defects and a hydroxide phase, which makes the structure of the active phase closer in composition to hydroxylated indium oxide nanoparticles $In_2O_{3-x}(OH)_y$. The obtained catalysts exhibit high activity in the hydrogenation of CO_2 to methanol, comparable to values reported in the literature. Catalyst In–PAF-20 demonstrated the highest methanol production rate at temperatures below 300°C and pressures below 60 atm (435 $mg_{MeOH}\ g_{In}^{-1}\ h^{-1}$ at 60 atm, 275°C); however, this trend shifted in a subcritical ethanol where In–PAF-20-NH_2 exhibited higher methanol production rate (507 $mg_{MeOH}\ g_{In}^{-1}\ h^{-1}$ at 60 atm, 350°C). Both catalysts retained their activity over five reuse cycles, although a significant increase in the average particle size of the active phase was observed for In–PAF-20-NH_2.

In conclusion, PAFs are promising supports for the development of In-based CO_2 hydrogenation catalysts. At the same time, the investigation of further targeted modification of the catalysts, for example, by promoting the active phase or by incorporating other functional groups into the support structure, remains essential to enhance their activity.

References

1. Ye J, Dimitratos N, Rossi LM, et al (2025) Hydrogenation of CO 2 for sustainable fuel and chemical production. Science (80-) 387:. https://doi.org/10.1126/science.adn9388
2. Hepburn C, Adlen E, Beddington J, et al (2019) The technological and economic prospects for CO2 utilization and removal. Nature 575:87–97. https://doi.org/10.1038/s41586-019-1681-6
3. Schaub T (2018) CO2-based hydrogen storage: CO2 hydrogenation to formic acid, formaldehyde and methanol. Phys Sci Rev 3:1–14. https://doi.org/10.1515/psr-2017-0015
4. Dalena F, Senatore A, Marino A, et al (2018) Methanol Production and Applications: An Overview. Methanol Sci Eng 3–28. https://doi.org/10.1016/B978-0-444-63903-5.00001-7
5. Maximov AL, Beletskaya IP (2024) Carbon dioxide and “methanol” economy: advances in the catalytic synthesis of methanol from CO2. Russ Chem Rev 93:RCR5101. https://doi.org/10.59761/RCR5101
6. Tedeeva MA, Kustov AL, Batkin AM, et al (2024) Catalytic systems for hydrogenation of

CO2 to methanol. Mol Catal 566:114403. https://doi.org/10.1016/j.mcat.2024.114403

7. Araújo TP, Mitchell S, Pérez-Ramírez J (2024) Design Principles of Catalytic Materials for CO 2 Hydrogenation to Methanol. Adv Mater 36:1–22. https://doi.org/10.1002/adma.202409322
8. Martin O, Martín AJ, Mondelli C, et al (2016) Indium Oxide as a Superior Catalyst for Methanol Synthesis by CO 2 Hydrogenation . Angew Chemie 128:6369–6373. https://doi.org/10.1002/ange.201600943
9. Wang J, Zhang G, Zhu J, et al (2021) CO2Hydrogenation to Methanol over In2O3-Based Catalysts: From Mechanism to Catalyst Development. ACS Catal 11:1406–1423. https://doi.org/10.1021/acscatal.0c03665
10. Shi Z, Yang L, Lu Z, et al (2024) Comprehensive Insight into Indium Oxide-Based Catalysts for CO2 Hydrogenation: Thermal, Photo, and Photothermal Catalysis. Adv Funct Mater 34:1–27. https://doi.org/10.1002/adfm.202409904
11. Rassolov A V., Baeva GN, Melnikov DP, et al (2024) The impact of the porous structure on the efficiency of PdIn methanol synthesis catalysts. Mendeleev Commun 34:711–714. https://doi.org/10.1016/j.mencom.2024.09.028
12. Sharma P, Hoang Ho P, Shao J, et al (2023) Role of ZrO2 and CeO2 support on the In2O3 catalyst activity for CO2 hydrogenation. Fuel 331:125878. https://doi.org/10.1016/J.FUEL.2022.125878
13. Zhang X, Kirilin A V., Rozeveld S, et al (2022) Support Effect and Surface Reconstruction in In2O3/m- ZrO2 Catalyzed CO2 Hydrogenation. ACS Catal 12:3868–3880. https://doi.org/10.1021/acscatal.2c00207
14. Sorokina SA, Kuchkina N V., Mikhailov SP, et al (2023) Highly Selective CO2 Hydrogenation to Methanol over Complex In/Co Catalysts: Effect of Polymer Frame. Nanomaterials 13:. https://doi.org/10.3390/nano13232996
15. Karakhanov E, Maximov A, Terenina M, et al (2020) Selective hydrogenation of terminal alkynes over palladium nanoparticles within the pores of amino-modified porous aromatic frameworks. Catal Today 357:176–184. https://doi.org/10.1016/j.cattod.2019.05.028
16. Bazhenova MA, Kulikov LA, Makeeva DA, et al (2023) Hydrodeoxygenation of Lignin-Based Compounds over Ruthenium Catalysts Based on Sulfonated Porous Aromatic Frameworks. Polymers (Basel) 15:4618. https://doi.org/10.3390/polym15234618
17. Kulikov L, Kalinina M, Makeeva D, et al (2020) Palladium Catalysts Based on Porous Aromatic Frameworks, Modified with Ethanolamino-Groups, for Hydrogenation of Alkynes, Alkenes and Dienes. Catalysts 10:1106. https://doi.org/10.3390/catal10101106
18. Makeeva D, Kulikov L, Zolotukhina A, et al (2022) Functionalization strategy influences

the porosity of amino-containing porous aromatic frameworks and the hydrogenation activity of palladium catalysts synthesized on their basis. Mol Catal 517:112012. https://doi.org/10.1016/j.mcat.2021.112012

19. Makeeva DA, Kulikov LA, Oskina ED, et al (2022) Palladium Catalysts Based on Nitrogen-Containing Porous Aromatic Frameworks for Hydrogenation of Unsaturated Compounds. Pet Chem 62:1183–1194. https://doi.org/10.1134/S0965544122090092
20. Kulikov L, Dubiniak A, Makeeva D, et al (2024) Ruthenium catalysts based on porous aromatic frameworks synthesized by modified impregnation methods for hydrogenation of levulinic acid and its esters. Mater Today Sustain 25:100637. https://doi.org/10.1016/j.mtsust.2023.100637
21. Kulikov LA, Makeeva DA, Dubiniak AM, et al (2024) Hydrogenation of Furfural over Ruthenium Catalysts Supported on Porous Aromatic Frameworks. Pet Chem 64:471–479. https://doi.org/10.1134/S0965544124020191
22. Kulikov LA, Bazhenova MA, Bolnykh IS, et al (2024) Hydroconversion of Guaiacol Family Molecules Over Platinum Catalysts Based on Porous Aromatic Frameworks. Catal Letters 154:6106–6122. https://doi.org/10.1007/s10562-024-04793-w
23. Oskina E, Makeeva D, Kulikov L, Maximov A (2025) Copper Catalysts Supported on Porous Aromatic Frameworks for Hydrogenation of Ethylene Carbonate. Catal Letters 155:351. https://doi.org/10.1007/s10562-025-05200-8
24. Kulikov LA, Oskina ED, Maksimov AL, Karakhanov EA (2026) Palladium catalysts based on porous aromatic frameworks for hydrogenation of organic cyclic carbonates. Mendeleev Commun 36:220–222. https://doi.org/10.71267/mencom.7898
25. Makhova VA, Kulikov LA, Cherednichenko KA, et al (2025) Cu and Fe Catalysts Based on Porous Aromatic Frameworks for Oxidation of Alkylaromatics. Ind Eng Chem Res 64:143–157. https://doi.org/10.1021/acs.iecr.4c03159
26. Makhova VA, Kulikov LA, Akopyan A V., Karakhanov EA (2024) Molybdenum Catalysts Supported on Porous Aromatic Frameworks in Epoxidation of Olefins. Pet Chem 64:492–499. https://doi.org/10.1134/S0965544124020208
27. Wang H, Nenasheva M, Kulikov L, et al (2026) Heterogeneous Rh catalysts based on porous aromatic frameworks (PAFs) with N-containing functional groups for hydroformylation of olefins. Mol Catal 603:116292. https://doi.org/10.1016/j.mcat.2026.116292
28. Yue Y, Xiao H, Ke X, et al (2026) Reaction mechanism and structure-activity relationships of bimetallic catalysts for CO2 hydrogenation to methanol under vapor and liquid phase processes. J CO2 Util 105:103363. https://doi.org/10.1016/j.jcou.2026.103363

29. Wang D, Du Y, Liao Z, et al (2024) Liquid-phase CO2 hydrogenation to methanol synthesis: Solvent screening, process design and techno-economic evaluation. J CO2 Util 90:102976. https://doi.org/10.1016/j.jcou.2024.102976
30. Bai S-T, De Smet G, Liao Y, et al (2021) Homogeneous and heterogeneous catalysts for hydrogenation of CO 2 to methanol under mild conditions. Chem Soc Rev 50:4259–4298. https://doi.org/10.1039/D0CS01331E
31. Kothandaraman J, Dagle RA, Dagle VL, et al (2018) Condensed-phase low temperature heterogeneous hydrogenation of CO 2 to methanol. Catal Sci Technol 8:5098–5103. https://doi.org/10.1039/C8CY00997J
32. Kothandaraman J, Heldebrant DJ (2020) Towards environmentally benign capture and conversion: Heterogeneous metal catalyzed CO2 hydrogenation in CO2 capture solvents. Green Chem 22:828–834. https://doi.org/10.1039/c9gc03449h
33. Chen Y, Choi S, Thompson LT (2016) Low temperature CO2 hydrogenation to alcohols and hydrocarbons over Mo2C supported metal catalysts. J Catal 343:147–156. https://doi.org/10.1016/j.jcat.2016.01.016
34. Plietzsch O, Schilling CI, Tolev M, et al (2009) Four-fold click reactions: Generation of tetrahedral methane- and adamantane-based building blocks for higher-order molecular assemblies. Org Biomol Chem 7:4734–4743. https://doi.org/10.1039/b912189g
35. Yuan Y, Sun F, Ren H, et al (2011) Targeted synthesis of a porous aromatic framework with a high adsorption capacity for organic molecules. J Mater Chem 21:13498–13502. https://doi.org/10.1039/c1jm11998b
36. Merino E, Verde-Sesto E, Maya EM, et al (2014) Mono-functionalization of porous aromatic frameworks to use as compatible heterogeneous catalysts in one-pot cascade reactions. Appl Catal A Gen 469:206–212. https://doi.org/10.1016/j.apcata.2013.09.052
37. Lee YR, Chung YM, Ahn WS (2014) A new site-isolated acid-base bifunctional metal-organic framework for one-pot tandem reaction. RSC Adv 4:23064–23067. https://doi.org/10.1039/c4ra02683g
38. Yang J, Huang W, Liu Y, Zhou T (2018) Enhancing the conversion of ethyl levulinate to γ-valerolactone over Ru/UiO-66 by introducing sulfonic groups into the framework. RSC Adv 8:16611–16618. https://doi.org/10.1039/c8ra01314d
39. Barin G, Peterson GW, Crocellà V, et al (2017) Highly effective ammonia removal in a series of Brønsted acidic porous polymers: Investigation of chemical and structural variations. Chem Sci 8:4399–4409. https://doi.org/10.1039/c6sc05079d
40. Haldar R, Sikdar N, Maji TK (2015) Interpenetration in coordination polymers: Structural diversities toward porous functional materials. Mater Today 18:97–116.

https://doi.org/10.1016/j.mattod.2014.10.038

41. Shen JJ, Li MX, Wang ZX, et al (2014) Unexpected 4-fold [2 + 2] interpenetration and polycatenation behaviors in porous luminescent zinc metal-organic frameworks constructed from flexible 3,5-bis(4-pyridylmethoxy)benzoate ligand. Cryst Growth Des 14:2818–2830. https://doi.org/10.1021/cg500092t
42. Guan Q, Ni C, Yan T, et al (2024) Amine functionalized surface frustrated Lewis pairs boost CO2 photocatalysis. EES Catal 2:573–584. https://doi.org/10.1039/D3EY00261F
43. Avila-Montiel C, Tlahuext H, Ariza A, et al (2022) Indium Coordination Compounds Derived from Amino Amides. Eur J Inorg Chem 2022:. https://doi.org/10.1002/ejic.202200178
44. Akopyan A V., Arzyaeva N V., Lapteva A, et al (2026) Heterogeneous Peracid Catalysis over Sulfonated Porous Aromatic Frameworks for Ultradeep Oxidative Desulfurization of Straight-Run Gasoline. Ind Eng Chem Res 65:5419–5435. https://doi.org/10.1021/acs.iecr.5c05398
45. Koley P, Shit SC, Yoshida T, et al (2025) Metal organic framework derived In2O3/ZrO2 heterojunctions with interfacial oxygen vacancies for highly selective CO2-to-methanol hydrogenation. Nat Commun 16:8903. https://doi.org/10.1038/s41467-025-63932-y
46. Hoch LB, Wood TE, O'Brien PG, et al (2014) The Rational Design of a Single-Component Photocatalyst for Gas-Phase CO $_2$ Reduction Using Both UV and Visible Light. Adv Sci 1:1400013. https://doi.org/10.1002/advs.201400013
47. Detweiler ZM, Wulfsberg SM, Frith MG, et al (2016) The oxidation and surface speciation of indium and indium oxides exposed to atmospheric oxidants. Surf Sci 648:188–195. https://doi.org/10.1016/J.SUSC.2015.10.026
48. Panafidin MA, Bukhtiyarov AV, Prosvirin IP, et al (2022) A mild post-synthesis oxidative treatment of Pd-In/HOPG bimetallic catalysts as a tool of their surface structure fine tuning. Appl Surf Sci 571:151350. https://doi.org/10.1016/j.apsusc.2021.151350
49. Nemygina NA, Nikoshvili LZ, Matveeva VG, et al (2016) Pd-Nanoparticles Confined Within Hollow Polymeric Framework as Effective Catalysts for the Synthesis of Fine Chemicals. Top Catal 59:1185–1195. https://doi.org/10.1007/s11244-016-0639-2
50. Xie S, Zhang W, Lan X, Lin H (2020) CO2 Reduction to Methanol in the Liquid Phase: A Review. ChemSusChem 13:6141–6159. https://doi.org/10.1002/cssc.202002087
51. Ren M, Zhang Y, Wang X, Qiu H (2022) Catalytic Hydrogenation of CO2 to Methanol: A Review. Catalysts 12:403. https://doi.org/10.3390/catal12040403
52. Kothandaraman J, Heldebrant DJ, Lopez JS, Dagle RA (2023) Mechanistic insights to drive catalytic hydrogenation of formamide intermediates to methanol via deaminative

hydrogenation. Front Energy Res 11:1–7. https://doi.org/10.3389/fenrg.2023.1158499

53. Lu J, Boughner EC, Liotta CL, Eckert CA (2002) Nearcritical and supercritical ethanol as a benign solvent: polarity and hydrogen-bonding. Fluid Phase Equilib 198:37–49. https://doi.org/10.1016/S0378-3812(01)00754-3

The Figure Legend section

Fig.1 Schematic synthesis of PAFs obtained in current work

Fig.2 IR-spectra of PAFs obtained in this work

Fig.3 Nitrogen adsorption-desorption isotherms and pore size distribution graphs for PAF-20 and PAF-20-NH_2 materials

Fig.4 TEM microphotographs and particle size distribution graphs for **a** In–PAF-20, **b** In–PAF-20-NH_2

Fig.5 Nitrogen adsorption-desorption isotherms and pore size distribution graphs for In-PAF-20 and In-PAF-20-NH_2 catalysts

Fig.6 High resolution XPS spectra of **a** C 1s, **b** O 1s, and **c** In 3d for In-PAF-20

Fig.7 High resolution XPS spectra of **a** C 1s, **b** N 1s, **c** O 1s, and **d** In 3d for In-PAF-20-NH_2

Fig.8 Dependence of the methanol production rate of the In-PAF-20 catalyst in the CO_2 hydrogenation to methanol on **a** temperature at 40 atm, **b** pressure at 250°C, **c** water medium at 250°C, 40 atm; and **d** In content at 275°C, 40 atm. Reaction conditions: In–PAF-20 – 15 mg, solvent – 4.5 mL, CO_2/H_2 = 1:3, 6 h

Fig.9 TEM microphotographs and particle size distribution for In–PAF-20 (5 wt.% In)

Fig.10 Comparison of the methanol production rates of catalysts obtained in this work in the hydrogenation of CO_2 to methanol. Reaction conditions: catalyst – 15 mg, ethanol – 4.5 mL, CO_2/H_2 = 1:3, 6 h

Fig.11 The methanol production rates of obtained catalysts upon reuse. Reaction conditions: catalyst – 15 mg, ethanol – 4.5 mL, 275°C, 60 atm, CO_2/H_2 = 1:3, 6 h

Fig.12 TEM microphotographs and particle size distributions for **a** In–PAF-20, **b** In–PAF-20-NH_2 after the 5^{th} reuse cycle

Supplementary Files

This is a list of supplementary files associated with this preprint. Click to download.

- graphicalabstract.jpg